

# Performance of the Particle-Identification Silicon-Telescope Array Coupled with the VAMOS++ Magnetic Spectrometer

L. Bégué-Guillou<sup>a,b</sup>, A. Lemasson<sup>a,\*</sup>, P. Morfouace<sup>b,c</sup>, D. Ramos<sup>a</sup>, J. Taieb<sup>b,c</sup>, J.D. Frankland<sup>a</sup>, M. Rejmund<sup>a</sup>, G. Fremont<sup>a</sup>, P. Gangnant<sup>a</sup>, A. Cobo-Zarzuelo<sup>a</sup>, N. Kumar<sup>a</sup>, T. Efremov<sup>b,c</sup>, A. Chatillon<sup>b,c</sup>, E. Clément<sup>a</sup>, G. De France<sup>a</sup>, A. Francheteau<sup>a</sup>, I. Jangid<sup>a</sup>, C. Lenain<sup>b,c</sup>, B. Mauss<sup>b,c</sup>, T. Tanaka<sup>a</sup>, L. Audoin<sup>g</sup>, M. Caamano<sup>d</sup>, B. Errandonea<sup>d</sup>, M. Godio<sup>g</sup>, D. Gruyer<sup>f</sup>, B. Jacquot<sup>a</sup>, M. Lalande<sup>a</sup>, R. C. Malone<sup>h</sup>, A. Munoz<sup>d</sup>, A. P. D. Ramirez<sup>i</sup>, J. L. Rodríguez-Sánchez<sup>d</sup>, C. Schmitt<sup>e</sup>, O. Syrett<sup>b,c</sup>, C. Surrault<sup>b,c</sup>, A. P. Tonchev<sup>i</sup>

<sup>a</sup>GANIL, CEA/DRF-CNRS/IN2P3, F-14076, Caen, France

<sup>b</sup>CEA, DAM, DIF, F-91297, Arpajon, France

<sup>c</sup>Université Paris-Saclay, CEA, LMCE, F-91680, Bruyères-le-Châtel, France

<sup>d</sup>IGFAE – Universidade de Santiago de Compostela, E-15706, Santiago de Compostela, Spain

<sup>e</sup>Institut Pluridisciplinaire Hubert Curien, CNRS/IN2P3-UDS, F-67037, Strasbourg, France

<sup>f</sup>LPC Caen, ENSICAEN, Université de Caen, CNRS/IN2P3, F-14000, Caen, France

<sup>g</sup>IJCLab, Université Paris-Saclay, CNRS/IN2P3, F-91405, Orsay, France

<sup>h</sup>Volgenau Physics Department, United States Naval Academy, MD 21409, Annapolis, USA

<sup>i</sup>Nuclear and Chemical Sciences Division, LLNL, CA, 94550, Livermore, USA

## Abstract

The Particle-Identification Silicon-Telescope Array (PISTA) is a new detection system designed for high-resolution studies of fission process induced by multi-nucleon transfer in inverse kinematics. It is specifically optimized for experiments with the VAMOS++ magnetic spectrometer at GANIL (Grand Accélérateur National d’Ions Lourds). The array comprises eight trapezoidal  $\Delta E$ - $E$  silicon telescopes arranged in a corolla configuration. Each telescope integrates two single-sided stripped silicon detectors, enabling target-like recoil identification, energy loss measurements, and trajectory reconstruction. Positioned in close proximity to the target, PISTA’s compact geometry achieves high-efficiency tracking of target-like recoils produced in multi-nucleon transfer reactions at Coulomb barrier energies. The spatial segmentation of the array allows precise determination of the mass and charge of the target-like nucleus, and excitation energy of fissioning systems. This work presents the particle identification and excitation energy reconstruction performances for the interactions of  $^{238}\text{U}$  beam with  $^{12}\text{C}$  target. An excitation energy resolution of 870 keV (FWHM) was determined together with mass resolution of 1.1 % (FWHM). The combination of PISTA and VAMOS++ magnetic spectrometer enables unprecedented investigations of the fission process as a function of the excitation energy of the fissioning nucleus, particularly for exotic systems produced in transfer-induced reactions.

## 1. Introduction

A thorough comprehension of the fission process necessitates an in-depth understanding of the influence of nuclear properties and the characteristics of the reaction entrance channel on the evolution of the fissioning system from its initial configuration to the formation of fission fragments. The excitation energy ( $E^*$ ) of the fissioning system significantly influences both the probability of fission and the characteristics of the resulting fragments. Measurements of fission observables as a function of  $E^*$  provide crucial insights into the interplay between nuclear structure effects, dissipation, and the dynamics of the large-amplitude deformation process leading to scission [1]. The evolution of fission fragment yields and fission probabilities with respect to excitation energy is significant for

both fundamental nuclear physics investigations, encompassing the study of shell effects and their damping as excitation increases, and practical applications within the nuclear industry, such as reactor design and waste transmutation.

Systematic studies of fission probabilities [2–4] and fragment yields [5–8] as function of  $E^*$  for various compound nuclei across the nuclear chart are fundamental to constrain theory, including model ingredients such as level densities, barrier heights, and the role of shell effects. Provided that the fissioning system and its excitation energy can be measured event-by-event, multi-nucleon transfer induced reactions are ideal to that goal, since several systems can be studied in a single experiment [3, 4, 6, 7, 9, 10].

Traditionally, isotopic yields have been measured using thermal neutron-induced fission reactions in setups such as the Lohengrin spectrometer [11, 12]. However, such methods often suffer from limited resolution in fission fragment charge identification, restricting access to isotopic yields

\* Corresponding author

E-mail address [antoine.lemasson@ganil.fr](mailto:antoine.lemasson@ganil.fr) (A. Lemasson)

only for the light fission fragment. The challenges are even greater with non-thermal neutron beams, due to a significant reduction in the available neutron flux and a decreased fission rates. Recent experimental programs employing fast neutron beams [13, 14] aimed to address these challenges by measuring fission fragment yields as a function of neutron energy. Alternatively, cumulative fission fragment yields have been measured via activation technique combined with high-resolution  $\gamma$ -ray spectroscopy following irradiation at different incident neutron energies [15–17].

In the last decades, elemental and later isotopic yields with high resolution have been measured using Coulomb-excitation reactions in inverse kinematics with fast radioactive beams at GSI using the FRS spectrometer and SOFIA [18–20]. While this method provides unique access to a wide range of systems, the excitation energy of the fissioning nucleus cannot be determined on an event-by-event basis. Alternatively, in multi-nucleon transfer reactions at energies around the Coulomb barrier, the fissioning system is produced as a heavy partner, and its properties such as mass, atomic number, and excitation energy can be inferred from the measurement of the complementary, light partner. In Refs [3, 5, 6, 21], multi-nucleon transfer in a direct-kinematics framework were employed to identify the fissioning system and to extract its excitation energy. However, in direct kinematics, complete isotopic identification of the fission fragments cannot be achieved.

The combination of inverse kinematics, and multi-nucleon transfer reactions enables the simultaneous measurement of entrance channel properties and isotopic identification of fission fragments. This approach was initially implemented at the VAMOS++ spectrometer at GANIL [22] using the SPIDER silicon telescope array where isotopic yields and fission probabilities were reported in Refs. [4, 7, 9, 10]. However the fissioning system excitation energy resolution and target-like recoil isotopic separation were constrained by the design of the target-like recoil detection system, i.e SPIDER array, specifically its insufficient spatial granularity.

To address these limitations, a new detection system, PISTA (Particle Identification Silicon Telescope Array), was developed for the measurement and characterization of target-like recoils from multi-nucleon transfer reactions. PISTA enables isotopic identification of the coincident reaction partner nucleus (which may undergo fission) and a precise determination of its excitation energy. The implementation with the VAMOS++ spectrometer, which provides isotopic identification of fission fragments, allows the correlation of the entrance and exit channels of the reaction on an event-by-event basis. This capability allows for more precise studies of fission probabilities and fission fragment yields as a function of  $E^*$  for a wide range of systems.

This paper presents a characterization of the PISTA device, detailing its design, construction, and performances. Notably, it highlights the device's capability

of achieving high-precision isotopic separation, accurate excitation-energy reconstruction, and its suitability for operation in inverse kinematic configurations, which are particularly advantageous for studies of the fission process.

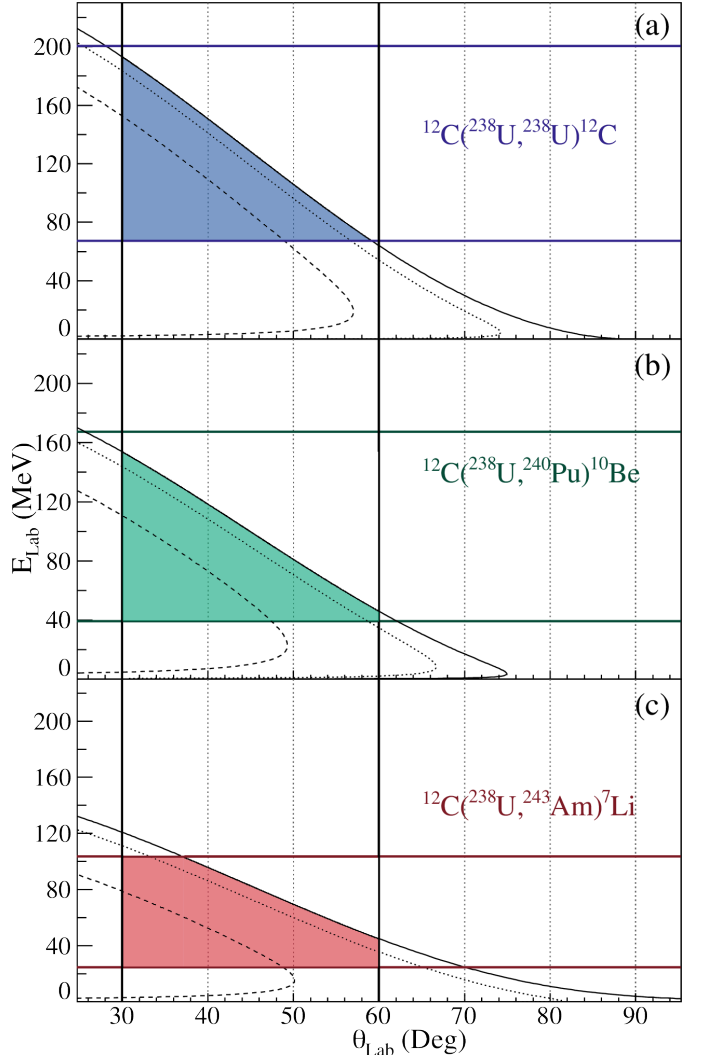


Figure 1: Calculations for the reactions in inverse kinematics (a)  $^{12}\text{C}(^{238}\text{U}, ^{238}\text{U})^{12}\text{C}$ , (b)  $^{12}\text{C}(^{238}\text{U}, ^{240}\text{Pu})^{10}\text{Be}$ , and (c)  $^{12}\text{C}(^{238}\text{U}, ^{243}\text{Am})^7\text{Li}$ , where a  $^{238}\text{U}$  beam at 5.95 MeV/A is bombarding a  $^{12}\text{C}$  target. The distinct curves illustrate the laboratory energy-angle correlation of the recoiling target-like nucleus for reactions resulting in the ground state (solid line) and excited states at  $E^* = 5$  MeV (dotted line) and  $E^* = 20$  MeV (dashed line) in the beam-like heavy ejectile. The vertical lines denote the angular range encompassed by PISTA, while the horizontal lines correspond to the energy constraint necessary for complete identification (i.e., events where the target-like ions are stopped in the second stage of the silicon telescope).

## 2. Detection requirements

The primary objective of the described setup is to use two-stage silicon telescopes and apply the  $\Delta E$ - $E$  technique to isotopically identify target-like nuclei spanning the

range from helium to oxygen produced in multi-nucleon reactions in inverse kinematics. The excitation energy of the fissioning system is inferred using the missing-mass method [23]. This calculation assumes that the target-like fragment is not excited and that all excitation energy is contained within the fissioning system. Accurate application of the missing-mass method requires precise determination of the scattering angle ( $\theta_{lab}$ ) and the kinetic energy ( $E_{lab}$ ) of the target-like residue.

Figure 1 illustrates the calculated typical kinematical correlation between the kinetic energy of a target-like residue and its laboratory angle. The reactions are induced by a  $^{238}\text{U}$  beam at a bombarding energy of 5.95 MeV/A on a  $^{12}\text{C}$  target. Panels (a)-(c) represent three distinct reaction channels of interest, as follows: (a)  $^{12}\text{C}(^{238}\text{U}, ^{238}\text{U})^{12}\text{C}$ , (b)  $^{12}\text{C}(^{238}\text{U}, ^{240}\text{Pu})^{10}\text{Be}$ , and (c)  $^{12}\text{C}(^{238}\text{U}, ^{243}\text{Am})^{7}\text{Li}$ . The distinct curves illustrate the laboratory energy-angle correlation of the target-like nucleus for reactions resulting in various excitation energy ( $E^*$ ) within the beam-like projectile.

To fully identify target-like recoils in a two-stage silicon telescope and reconstruct their kinetic energies, ions must possess sufficient energy to traverse the first stage ( $\Delta E$ ), while remaining low enough in energy to stop within the second stage ( $E$ ). This requirement, intimately linked to the thicknesses of the two stages, defines the corresponding accessible energy intervals as illustrated by the horizontal lines in Figure 1. A critical design requirement was to prevent fission fragments from interacting with the silicon detector array, which would both hinder identification and pose a risk of damage to the silicon detectors. Fission fragments emitted in-flight for all reactions of interest are confined to a cone of less than  $30^\circ$ , which defines the inner angular limits of the detector array. The vertical lines in Figure 1 denote the angular range encompassed by PISTA, while the shaded regions indicate the angular and energy phase space accessible for each reaction.

A high-resolution isotopic identification necessitates a uniform effective thickness across a broad angular range in the first detection stage ( $\Delta E$ ). In previous studies employing the SPIDER array [4, 7, 10], the detector was positioned perpendicular to the beam axis, resulting in a significant variation in effective thickness as a function of the polar angle of reaction products. This variation posed a particular challenge along with large strip sizes. Consequently, segmented detectors with a thickness uniformity better than 1 % and a detector surface oriented nearly perpendicular to the particle trajectory are essential to minimize the dependence of the effective detector thickness on the particle's incident angle..

Furthermore, PISTA aims to enhance the excitation-energy resolution compared to previous studies conducted using the SPIDER annular silicon detection system. In these studies, an excitation-energy resolution of 2.7 MeV (FWHM) was reported [4, 7, 10]. The excitation-energy resolution of the fissioning system is primarily determined by the accuracy of the scattering-angle determination

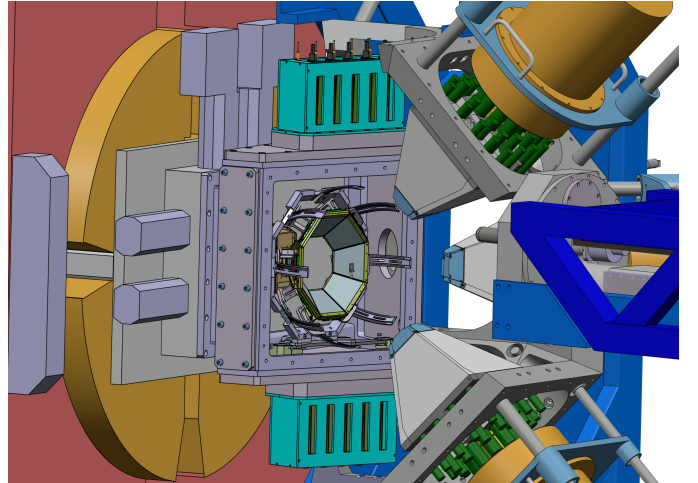


Figure 2: Three-dimensional representation of the PISTA detection system is depicted, positioned around the target location in front of the VAMOS++ spectrometer [22]. Three EXOGAM HPGe clover detectors [25] are placed at backward angles.

and the target thickness. The beam spot size, typically  $\sigma_x \sim 0.6$  mm and  $\sigma_y \sim 1$  mm, exceeds the intended detector strip size of 0.535 mm. Consequently, determining the scattering angle necessitates both the interaction position in PISTA detector and the beam interaction position on the target. The beam interaction position can be determined with an uncertainty of 0.24 mm using the Dual Position Sensitive Multi-Wire Proportional Counter (DPS-MWPC) tracking detector used with VAMOS++ [24]. To achieve an excitation-energy resolution better than 1 MeV, the required angular resolution must not exceed  $0.18^\circ$ , and the energy resolution must not exceed 800 keV (including uncertainty on the reaction position in the target). Furthermore, a substantial solid angle should be encompassed to compensate for the relatively small cross sections of the channels of interest.

To fulfill these requirements, we implemented an array of single-sided silicon-strip  $\Delta E-E$  telescopes in a corolla configuration, which is detailed in the subsequent section.

### 3. PISTA telescopes

The PISTA detection system comprises eight trapezoidal telescopes arranged in a flower-like corolla geometry, as illustrated in Figure 2. The figure presents a three-dimensional perspective of the PISTA array positioned around the target location in front of the VAMOS++ spectrometer. PISTA's telescopes comprise two silicon stages separated by a 4.5 mm gap. Furthermore, the setup includes three EXOGAM HPGe clover detectors [25] placed at backward angles.

#### 3.1. First stage: $\Delta E$ single-sided detector

The  $\Delta E$  detectors were manufactured by Micron Semiconductor Ltd. using n-type silicon and mounted on cus-

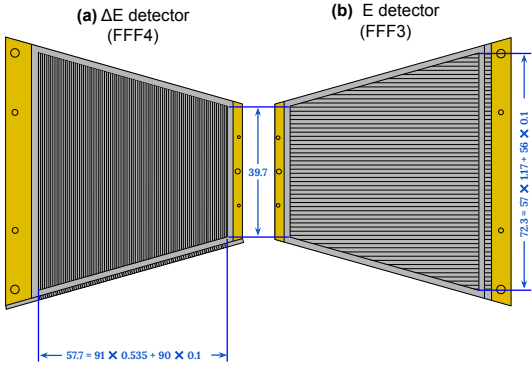


Figure 3: Drawing of the front side of (a)  $\Delta E$  (FFF4 design) and (b)  $E$  (FFF3 design) manufactured by Micron Semiconductor Ltd.

tom circuit boards designed at GANIL. Figure 3(a) depicts a schematic representation of the front segmented side of the  $\Delta E$  stage. The detectors have a trapezoidal shape, with their long and short bases measuring 39.74 mm and 72.29 mm, respectively, resulting in an active area of approximately  $27.5 \text{ cm}^2$ . Depending on the telescope configuration, the detectors possess thicknesses ranging between  $100 \mu\text{m}$  and  $108 \mu\text{m}$ , with a uniformity better than 1%. The entrance side of the detectors is segmented into 91 strips (as illustrated in Figure 3). The  $535 \mu\text{m}$  wide strips are separated by  $100 \mu\text{m}$  passive inter-strips. Due to the geometry, the strips exhibit variable dimensions, leading to variable capacitance values ranging between 22.3 and 40.1 pF. It is noteworthy that particular attention was given to the bounding and routing of the strips, which are fabricated on the detector's side, to minimize the loss of solid angle. The rear side is single-readout and serves to polarize the junction with a nominal bias of 20 V. The entrance and exit windows consist of  $0.5 \mu\text{m}$  aluminum, selected to minimize the energy loss of particles within this dead layer. The intrinsic energy resolution of the strips and the rear side will be presented in Section 5.

### 3.2. Second stage: $E$ single-sided detector

The  $E$  detectors were manufactured by Micron Semiconductor Ltd. using n-type silicon and mounted them on custom circuit boards designed at GANIL. Figure 3(b) depicts a schematic view of the front segmented side of the  $E$  stage. The detectors share the same trapezoidal shape and dimensions as the  $\Delta E$  detectors, but with a slightly larger active area of approximately  $29.9 \text{ cm}^2$ . The second stage of the PISTA telescopes has a typical thickness of 1 mm. The entrance side of the detectors is segmented into 57 vertical strips (as shown in Figure 3). The  $1.17 \mu\text{m}$  wide strips are separated by  $100 \mu\text{m}$  passive inter-strips. Due to the geometry, the strips have variable lengths, resulting in variable capacitance ranging between 0.2 and 7.0 pF. The rear side is single readout and is utilized to polarize the junction with a nominal bias of 190 V. Similar to  $\Delta E$  detectors, an aluminum entrance window of  $0.5 \mu\text{m}$  was

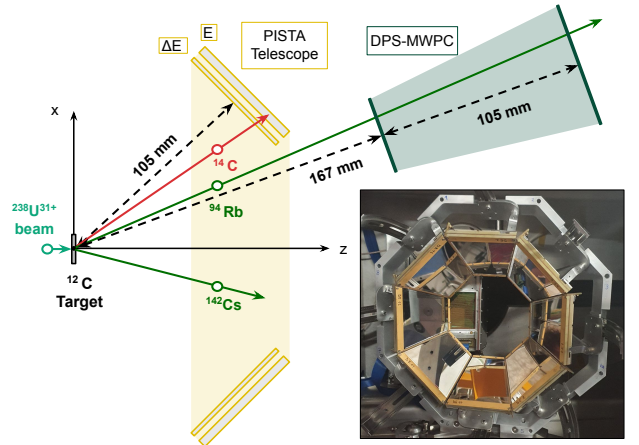


Figure 4: Schematic top view of the detection systems surrounding the  $^{12}\text{C}$  target. The PISTA array, comprising  $\Delta E - E$  telescopes (illustrated in yellow), and the DPS-MWPC (illustrated in green) are depicted. A representative reaction scenario is presented for the  $^{12}\text{C}(^{238}\text{U},^{236}\text{U})^{14}\text{C}$  transfer reaction, followed by the fission of  $^{236}\text{U}$  into two fragments, specifically  $^{94}\text{Rb}$  and  $^{142}\text{Cs}$ , and the detection of  $^{14}\text{C}$  in PISTA. The inset provides a photograph of the PISTA experimental setup.

employed. The intrinsic energy resolution of the strips and rear side will be presented in Section 5.

### 3.3. Mechanical assembly

Figure 4 illustrates a schematic implantation of the PISTA array and the DPS-MWPC in front of the VA-MOS++ spectrometer, with the relative distances to the  $^{12}\text{C}$  target indicated. The telescopes are mounted on a dedicated holding structure designed to facilitate versatile, reproducible, and precise positioning of the telescopes. In the nominal configuration, the detectors form a closed corolla around the beam axis, with each telescope entrance window centered 105.5 mm away from the target. Each telescope is oriented such that the normal to its center subtends a polar angle of  $45^\circ$  relative to the beam axis at the target position. In this configuration, the PISTA array covers laboratory polar angles ranging from  $30^\circ$  to  $60^\circ$ . Given the positioning and segmentation of the detector, the expected uncertainties for the target-like trajectory angles are approximately  $\sigma(\theta_{lab}) \approx 0.12^\circ$  for the polar angle and  $\sigma(\phi_{lab}) \approx 0.3^\circ$  for the azimuthal angle. This configuration provides suitable angular coverage for target-like recoils while allowing fission fragments to pass through the central aperture up to angles of  $\theta \sim 30^\circ$ . Furthermore, to enable future versatile use of the array for a wider range of kinematics, each telescope can be moved individually by steps of  $1^\circ$  from  $45^\circ$  to  $90^\circ$ . This modification can be further combined with a change in the installation radius, which is adjusted by utilizing different spacer-mounting components corresponding to predefined radii of 105.5 mm, 125.5 mm, and 145.5 mm. The target is typically surrounded by permanent magnets ( $B = 50 \text{ mT}$ )

that collect  $\delta$  electrons produced in the interaction of the beam with the target.

## 4. Electronics and data acquisition

The Data Acquisition (DAQ) system, detector signal digitization, and event building are managed by commercial modules from Mesytec GmbH & Co. The entire electronics setup is housed within a single VME crate, following an implementation similar to that reported in Ref. [26]. A comprehensive overview of the hardware connections and PISTA architecture is provided in Figure 5.

### 4.1. Readout electronics

Charge signals from both the front (strips) and rear sides of each telescope detector are processed and recorded through a dedicated chain of electronic modules.

#### 4.1.1. Rear-side detectors

The 16 rear-side signals (8  $\Delta E$  and 8  $E$ ) are routed to custom charge-sensitive preamplifiers (CSP) developed by CEA-DAM. These CSPs were specifically designed for the plain rear-side electrodes of the PISTA detectors.

- $\Delta E$  detectors: the  $100 \mu\text{m}$   $\Delta E$  detectors exhibit a high output capacitance ( $> 4 \text{nF}$ ), which typically degrades energy resolution. To mitigate this, the  $\Delta E$  CSP utilizes three JFETs in parallel to achieve a high input transconductance of  $120 \text{ mS}$ , significantly higher than standard commercial units. A high-bandwidth decompensated operational amplifier in the cascade stage ensures a closed-loop bandwidth of  $3 \text{ MHz}$ ,
- $E$  detectors: these detectors have a standard capacitance of approximately  $400 \text{ pF}$ . A similar CSP topology is used but with a single JFET, resulting in a transconductance of  $45 \text{ mS}$  and a closed-loop bandwidth of  $10 \text{ MHz}$ .

Digital signal processing and pulse amplitude encoding are performed by two MDPP-16 SCP modules [27], one for each detector type. Within the MDPP, signals are split into two branches:

- amplitude branch: uses a trapezoidal filter (shaping time  $1.2 \mu\text{s}$  for both  $\Delta E$  and  $E$ ) to capture and hold the signal peak,
- trigger branch: extracts timing information via a Constant Fraction Discriminator (CFD); for  $\Delta E$ , the shaping time is  $1.2 \mu\text{s}$  and for  $E$ , it is reduced to  $0.2 \mu\text{s}$ .

The filters are configured without a flat top, resulting in a triangular output. Signals are only processed if the CFD output falls within a "window of interest" (width and offset adjustable) relative to a reference trigger. While these modules can operate in self-triggering mode, PISTA utilizes an external validation signal.

### 4.1.2. Front stripped side detectors

The 1184 strip signals are routed to ten Mesytec Multiplexed Readout (MMR) modules [28] (four for  $E$ , six for  $\Delta E$ ). Each MMR handles up to 128 channels and performs pre-amplification, digitization, and trigger generation.

The integrated Charge Sensitive Amplifiers (CSA) are ranged for maximum expected energy depositions:  $2.7 \text{ pC}$  (60 MeV) for  $\Delta E$  and  $9 \text{ pC}$  (200 MeV) for  $E$ . Following the CSA, the signal is split:

- energy branch: shaped at  $500 \text{ ns}$  and passed to a stretcher,
- trigger branch: shaped at  $160 \text{ ns}$  and sent to a leading-edge discriminator.

The 128 amplitude signals are multiplexed across four 50 MHz ADCs (4096 channels). An internal FPGA buffers the digitized data and transmits them to VMMR-8 VME modules [28], which handle de-multiplexing and data formatting. Similar to the MDPP modules, the VMMR validates signal readout based on a specific window of interest.

### 4.2. Data acquisition trigger

The VME crate is controlled by an MVLC module [29], an FPGA-based controller designed for high-rate data readout. The primary PISTA trigger is defined as a logical OR of the rear  $E$  detector CFD outputs from the MDPP.

For coincidence experiments, a global trigger is constructed from the logical OR of several sources:

- PISTA standalone,
- PISTA and VAMOS++ coincidence (generated from the DPS-MWPC detector and the PISTA  $E$  signals) using a  $100 \text{ ns}$  window.

To manage high rates, the PISTA trigger can be down-scaled by a factor  $D$ . Triggers are validated only if the system is not in "dead time." Total dead time includes signal processing ( $\sim 7-8 \mu\text{s}$ ) and readout ( $\sim 6-7 \mu\text{s}$ ). Validated triggers are distributed by the MVLC to all modules to open their respective windows of interest (typically  $1 \mu\text{s}$  for MMR and  $0.5 \mu\text{s}$  for MDPP).

### 4.3. Data acquisition and coupling with other data acquisition systems

PISTA is integrated into the GANIL ecosystem via the NARVAL data flow system [30]. Multi-detector synchronization is achieved using the GTS common clock system [31], allowing PISTA to couple with VAMOS++ and EXOGAM (NUMEXO2 digitizers [32]).

A TGV (Trigger Générique VME) module in the PISTA crate receives validated triggers from the MVLC and requests a 48-bit, 10 ns resolution timestamp from the GTS BEAST. This timestamp is appended to the data of each Mesytec module for every event. More details on the implementation can be found in Ref. [26].

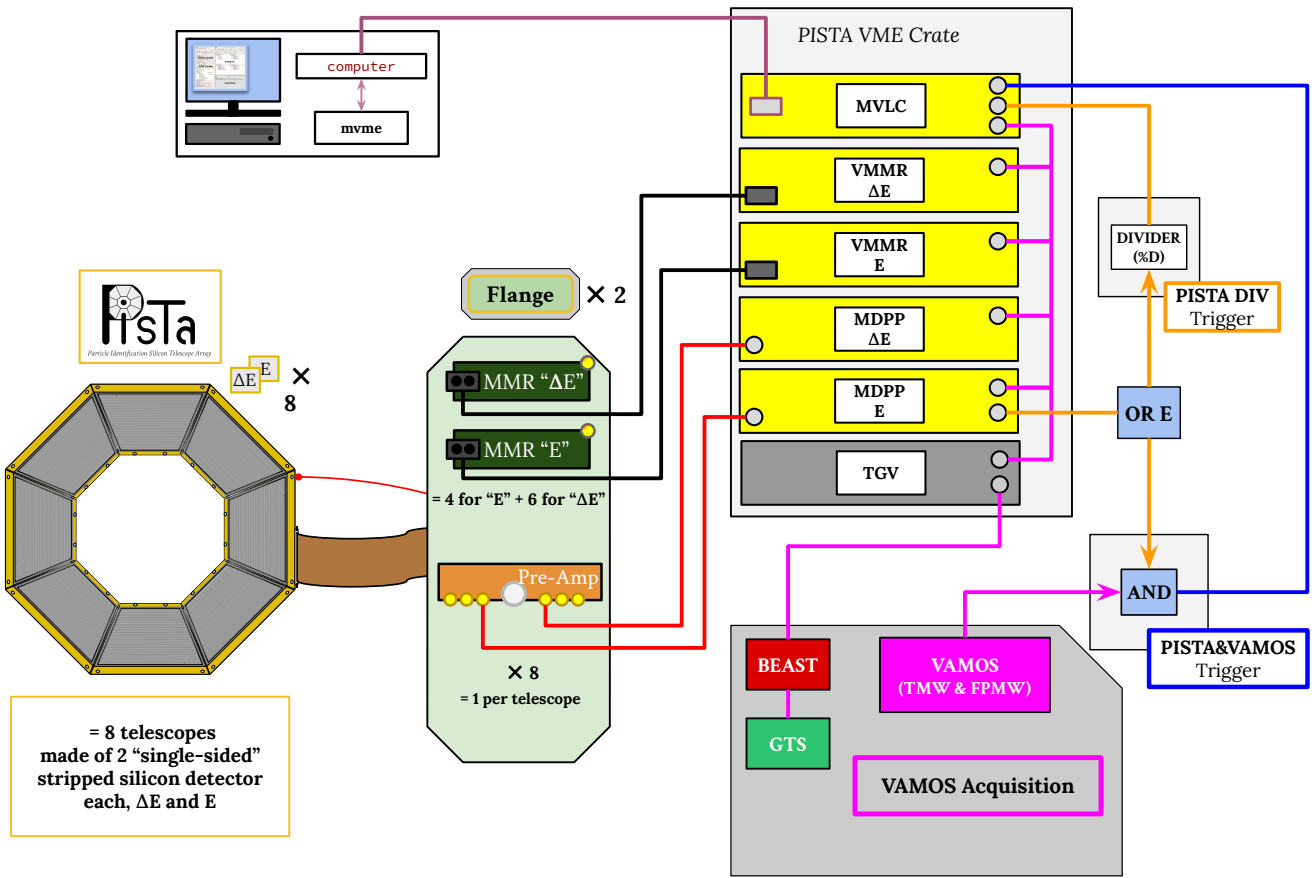


Figure 5: Overview of the PISTA hardware connections. On the left, a diagram illustrates the detector array, showing a single  $E$  detector connected and for half of the front side. The front-side readout is achieved via a flat cable (brown), while the rear side is connected using a single coaxial cable (red), which also serves as the bias voltage input. A schematic representation of one electronic flange is provided, including a  $\Delta E$  MMR and a  $E$  MMR module and a preamplifier (Pre-Amp). Each module is annotated with typical operating values. On the right, the VME crate dedicated to signal processing is shown, containing all essential modules used for the acquisition and digitization of the detector signals. Additionally, in the bottom right corner, the crates responsible for generating the trigger logic are displayed, along with the associated electronic modules.

Data are initially read via mvme software [33] and published over the network using ZeroMQ. A software transceiver converts these data into the MFM (MultiFrame Metaformat), embedding the timestamp in the header. These frames are then injected into NARVAL, where the MFMMerger [34] builds global events using a  $1\ \mu\text{s}$  coincidence window.

## 5. Characterization of the intrinsic energy detector resolution using radioactive sources

Detectors were characterized using  $3\alpha$  calibration sources. For the  $\Delta E$  detectors, energy resolution was measured to be approximately  $\sigma \sim 40$  keV and  $\sigma \sim 80$  keV at  $\sim 5.5$  MeV for the strips and the rear side, respectively. The difference can be attributed to the substantial capacitance of the rear side  $\Delta E$ . For the  $E$  detector, energy resolution was measured to be approximately  $\sigma \sim 40$  keV (limited by the resolution of the MMR ADC for the 200 MeV

range) and  $\sigma \sim 18$  keV at  $\sim 5.5$  MeV for the strips and the rear detector, respectively.

## 6. Performances using reactions in inverse kinematics

The performances of the PISTA detector under realistic conditions were determined during an experiment conducted at the GANIL facility in Caen, France. The data presented herein was derived from the E850 experimental dataset [35].

The PISTA array was positioned in front of the VAMOS++ spectrometer at a distance of 105 mm from the  $100\ \mu\text{g}/\text{cm}^2$  natural Carbon target. The target was bombarded by a  $5.95\ \text{MeV}/\text{A}$   $^{238}\text{U}$  beam with an intensity ranging between 0.1 and 2 pA. Fission was induced by multi-nucleon transfer reactions in inverse kinematics. The PISTA array was placed around the target at forward angles, symmetrically aligned around the beam axis, to detect target-like residues.

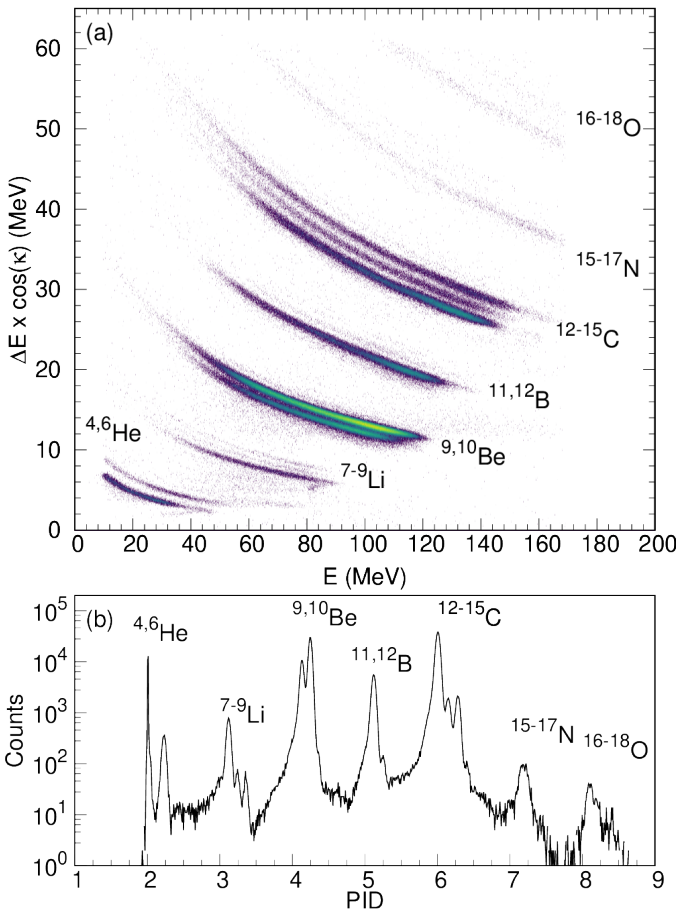


Figure 6: Particle identification obtained by PISTA array. In panel (a) the correlation between energy loss ( $\Delta E \times \cos(\kappa)$ ) and residual energy ( $E$ ) for events where the coincident fission fragments were detected in VAMOS++, is shown. In panel (b) the corresponding one-dimensional particle identification (PID) obtained from Deep Neural Network (see text). Different detected target-like isotopes are labeled.

Whenever the transfer reaction led to fission, the fragments were transmitted through the central aperture of PISTA to the VAMOS++ spectrometer, which was positioned at an angle of  $20^\circ$ . The DPS-MWPC detection system, located at the entrance of VAMOS++, enabled the event-by-event determination of the trajectory of fission fragments. This capability also allows the determination of the interaction position of the beam on the target.

### 6.1. Target-like recoil identification

In nuclear reactions occurring at energies close to the Coulomb barrier, multiple reaction channels become accessible. Consequently, unambiguous particle identification of the target-like recoil is essential to uniquely identify the fissioning system produced on an event-by-event basis. This objective was accomplished using the  $\Delta E - E$  method, which necessitates particle penetration until the second stage of the telescope. Thus, the thickness of the

$\Delta E$  detector determines the identifiable range of ions, encompassing helium to oxygen.

The  $\Delta E$  measurement was derived from the entrance-strip energy signals of the first stage, while the  $E$  measurement is obtained from the rear-side signals of the second stage. The energy loss ( $\Delta E$ ) was corrected for the difference of effective thickness of the detector ( $\cos(\kappa)$  where  $\kappa$  denotes the angle between the normal of the detection plane and the particle trajectory). The figure 6 illustrates the broad range of populated reaction channels. The resulting two-dimensional  $\Delta E - E$  correlation is presented in Figure 6(a) for three telescopes (with equivalent  $\Delta E$  thickness of  $103 \mu\text{m}$ ). Isotopic identification is achieved with high precision for ions up to oxygen. It should be noted that the nitrogen and oxygen isotopes originate mostly from reactions with contaminants.

A substantial enhancement in selectivity is evident when comparing the results obtained using the PISTA (Figure 6(a)) to the SPIDER (Figure 4 of Ref.[4]) setups. To quantify the improvement, the one-dimensional particle identification (PID) was extracted from the  $\Delta E - E$  correlation using a Deep Neural Network (DNN) trained on experimental data, following the procedure outlined in Ref. [36]. The resulting spectrum of PID is shown in Figure 6(b). A typical mass resolution of  $1.1\%$  (FWHM) for carbon isotopes was obtained, to be compared to  $8\%$  reported for SPIDER array. Utilizing these resolutions, comparison with Monte Carlo simulations indicates a pixel-level thickness non-uniformity of  $\sim 0.8\%$ .

### 6.2. Target-like recoil kinematics

The total energy of the light recoils was derived from the sum of  $\Delta E$  (obtained from the front side strip signal) and  $E$  (obtained from the rear side signal), and was corrected for energy loss in the target, entrance and exit dead layers of the detectors using energy loss tables [37]. In the data analysis, only events with a single strip multiplicity were considered. The scattering angles of the target-like recoils were inferred from the  $\Delta E$  and  $E$  strip position and the position of the interaction of the beam on the target. The information on the beam interaction position was obtained on an event-by-event basis when reactions lead to fission fragment detected in VAMOS++. For the events where no fission fragment was detected in VAMOS++, the average position of the beam (over the last 1000 events) was employed to correct for possible beam movements (typical beam spot size was  $0.6 \times 1 \text{ mm}^2$ ). A correlation of the energy and scattering angle for the target-like recoil  ${}^{10}\text{Be}$  measured in PISTA is shown in Figure 7(a) for the  ${}^{12}\text{C}({}^{238}\text{U}, {}^{240}\text{Pu}){}^{10}\text{Be}$  reaction. Figure 7(b) also shows the velocity of the  ${}^{240}\text{Pu}$  fissioning system as a function of its angle. It is noteworthy that the beam-like heavy reaction residue was not detected in VAMOS++, and the corresponding properties were systematically derived from the properties of the target-like recoil detected in PISTA. The calculated kinematic lines for  $E^* = 0$  and  $E^* = B_f$  are also shown in Figure 7.

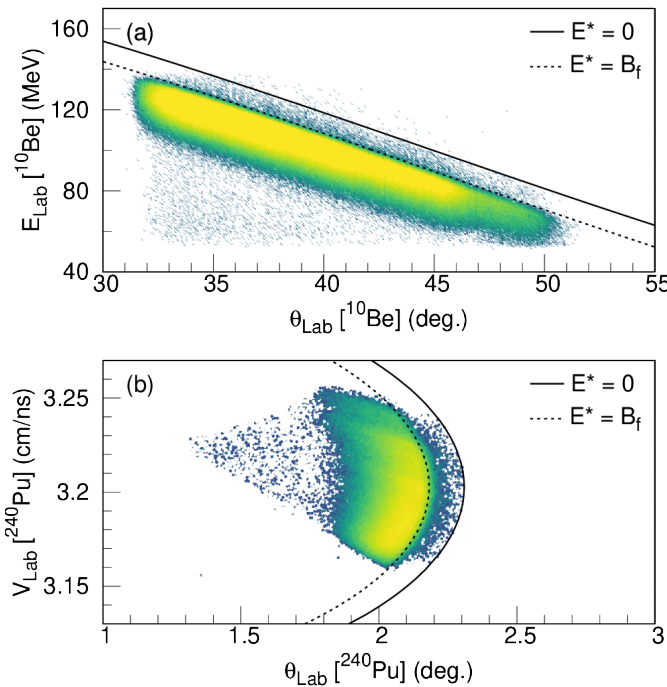


Figure 7: Kinematical correlations in the laboratory frame, measured for the  ${}^{12}\text{C}({}^{238}\text{U}, {}^{240}\text{Pu}){}^{10}\text{Be}$  reaction. Panel (a) illustrates the energy correlation with the angle of the target-like recoil  ${}^{10}\text{Be}$  detected in PISTA, while panel (b) illustrates the inferred correlation between the velocity and angle of the  ${}^{240}\text{Pu}$  fissioning system. The calculated kinematic lines for  $E^* = 0$  (full line) and  $E^* = B_f$  (dashed line) are also shown.

### 6.3. Reconstruction of the fissioning system excitation energy

The excitation energy of the fissioning system was determined using the missing-mass method [23], which employed the measurement of energy and angle of the target-like recoil. This approach assumes that the target-like nucleus is in its ground state and that all excitation energy is imparted to the fissioning system.

Figures 8 (a) and (b) depict the excitation energy spectra for reactions resulting in  ${}^{12}\text{C}$  and  ${}^{10}\text{Be}$  target-like recoils, respectively. The excitation energy resolution can be assessed using the elastic channel ( ${}^{12}\text{C}({}^{238}\text{U}, {}^{238}\text{U}){}^{12}\text{C}$  with  $E^* = 0$ ). A resolution of  $\sigma_E = 518(1)$  keV was determined by a gaussian fit on the left side of the elastic distribution to exclude the possible contribution from inelastic events. This value can be compared to  $\sigma_E = 1150(10)$  keV reported in the case of SPIDER array [4]. It is important to note that in the elastic channel  ${}^{238}\text{U}$  nuclei do not undergo fission, rendering it impossible to determine the beam interaction position on the target on an event-by-event basis. The average beam interaction position was employed to account only for average beam displacement, while the beam spread remained unaccounted for. Consequently, the newly reported resolution represents an upper limit for fission events.

Figure 8 (b) presents the reconstructed excitation en-

ergy spectra obtained for the  ${}^{12}\text{C}({}^{238}\text{U}, {}^{240}\text{Pu}){}^{10}\text{Be}$  channel. The red histogram shows the excitation energy distribution of  ${}^{240}\text{Pu}$  detected in PISTA in coincidence with a fission fragment in VAMOS++ corrected for the acceptance of the VAMOS++ spectrometer

$$N_{Fis} = N_V/a,$$

where:  $N_V$  is the number of  ${}^{10}\text{Be}$  nuclei detected in PISTA in coincidence with a fission fragment in VAMOS++ and  $a = 0.065$  is the simulated acceptance of VAMOS++. The black histogram shows the inclusive distribution in excitation energy for transfer events

$$N_{Tr} = N_{Fis} + N_{\bar{V}} \times D,$$

where:  $N_{\bar{V}}$  is the number of  ${}^{10}\text{Be}$  nuclei detected in PISTA with a downscaling factor  $D = 300$  for the PISTA experimental trigger, for which no fragments are detected in VAMOS. It can be seen from the Figure 8(b), that in this case, the 2p-transfer channel populates states in  ${}^{240}\text{Pu}$  up to approximately 16 MeV of excitation energy. The rapid increase of the fission probability obtained in coincidence with fission fragments in the vicinity of the fission barrier ( $B_f$ ) [38], indicated by the dashed line, can be utilized to infer excitation energy resolution.

Monte Carlo simulations were conducted to assess the various factors contributing to the obtained excitation energy resolution. The uncertainty in the energy of the reaction, attributed to the target thickness, accounts for  $\sigma = 170$  keV. The uncertainty in the target-like recoil interaction position within the PISTA array is responsible for  $\sigma = 190$  keV. The influence of the intrinsic energy resolution ( $\sigma_{\Delta E} \sim 40$  keV and  $\sigma_E \sim 18$  keV at 5.5 MeV) contributes to  $\sigma \sim 130$  keV. The beam spot position resolution of  $\sigma_{x,y} = 240 \mu\text{m}$  results in  $\sigma = 200$  keV. Consequently, the total uncertainty in excitation energy was determined to be  $\sigma_E \sim 370$  keV in the case of events detected in coincidence with a fission fragment, where beam interaction position on the target can be accurately determined on an even-by-event basis. In contrast, with the typical beam spot size of 0.5 mm without accounting for beam interaction position on the target, a resolution of  $\sigma_E \sim 500$  keV was obtained, which aligns with  $\sigma_E = 518(1)$  keV reported above for the elastic channel.

### 6.4. Target-like recoil coincidence with $\gamma$ rays

The PISTA array's mechanics was designed to facilitate its coupling to other detectors and in particular with the HPGe clover detectors of EXOGAM [25]. In the present experiment, three EXOGAM clovers were strategically positioned at backward angles of approximately  $135^\circ$ , situated at a distance of 120 mm from the target.  $\gamma$ -ray addback technique was employed to ensure the recovery of complete energy deposits within the EXOGAM clover detectors. The highest energy deposit within each segment served as the basis for determining the  $\gamma$ -ray detection angle. The measured  $\gamma$ -ray energy was corrected for Doppler

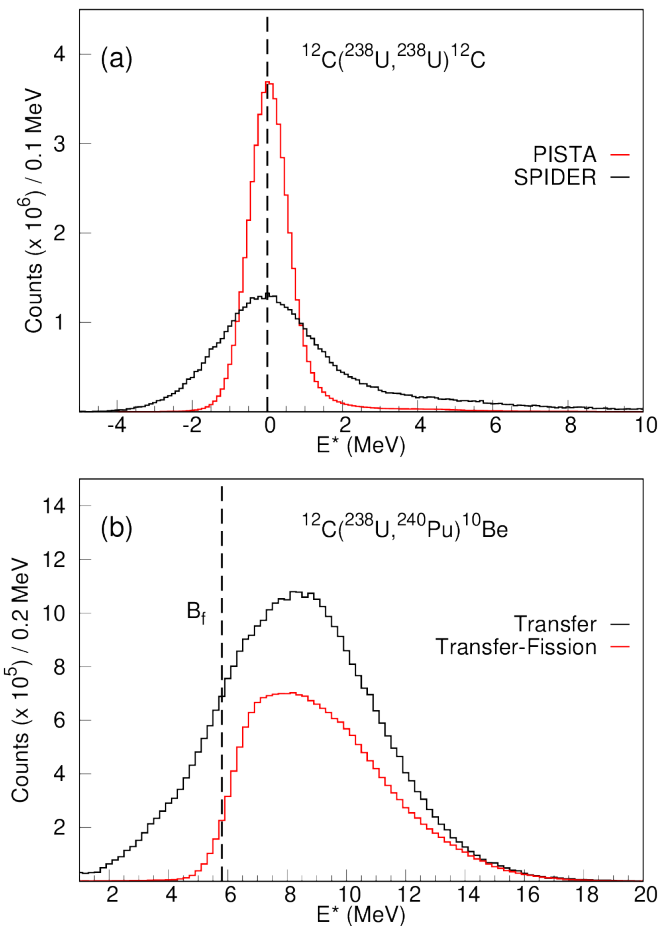


Figure 8: Reconstructed excitation energy spectra. Panel (a) illustrates a comparison of the excitation energy spectra in the  $^{12}\text{C}(^{238}\text{U}, ^{238}\text{U})^{12}\text{C}$  elastic channel obtained with PISTA array (red line) and SPIDER array (black line) [4]. Panel (b) shows the excitation energy spectra for the  $^{12}\text{C}(^{238}\text{U}, ^{240}\text{Pu})^{10}\text{Be}$  reaction channel for inclusive transfer reaction events (black line) and transfer reaction in coincidence with fission events detected in VAMOS++ (red line). See text for further details. The energy of the fission barrier ( $B_f = 5.6$  MeV [38]) is indicated by a dashed line.

effects event-by-event using the velocity vector measured with PISTA, in order to obtain the corresponding  $\gamma$ -ray spectrum emitted by the target-like recoil.

Figure 9(a) depicts the Doppler-corrected  $\gamma$ -ray spectrum of events in coincidence with  $^{10}\text{Be}$ . The first excited state of  $^{10}\text{Be}$ , characterized by an energy of  $E_\gamma(2^+) = 3.368$  MeV, is evident in the spectrum, thereby demonstrating that  $^{10}\text{Be}$  can be populated in its excited states in the  $^{12}\text{C}(^{238}\text{U}, ^{240}\text{Pu})^{10}\text{Be}$  reaction; which is consistent with the results of Ref. [4]. Figure 9(b) depicts the distribution of excitation energy in  $^{240}\text{Pu}$ , assuming  $^{10}\text{Be}$  was populated in its ground state, measured in coincidence with the 3.368 MeV transition. The spectrum was obtained using  $\gamma$ -ray gating region highlighted in Figure 9(a) by the red shaded area, with background subtraction. The black and red lines represent, respectively, the distributions of excitation energy measured for transfer and transfer-induced fission

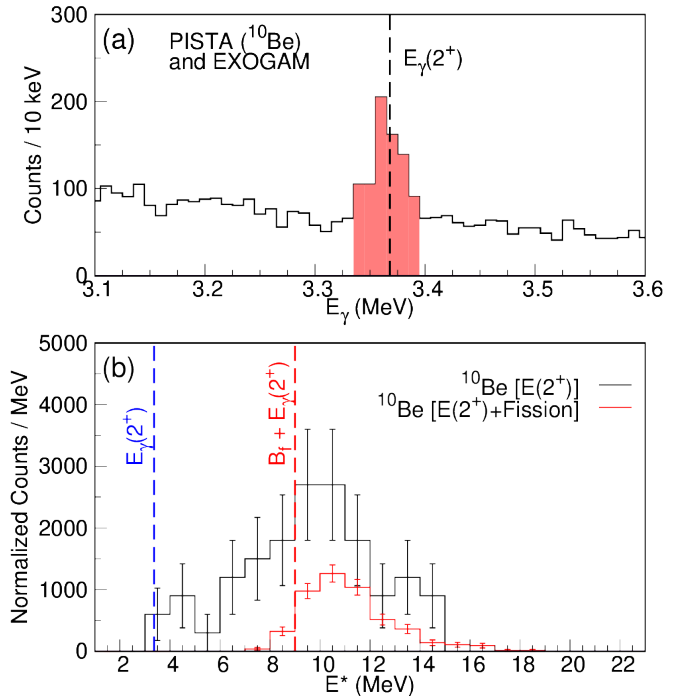


Figure 9: Coincidences with  $\gamma$  rays. Panel (a) illustrates the Doppler-corrected-  $\gamma$ -ray spectra measured by EXOGAM in coincidence with  $^{10}\text{Be}$  detected in PISTA. The energy of the first excited state,  $E_\gamma(2^+) = 3.368$  MeV, is indicated by a dashed line. The red shaded area illustrates the gate used for the coincidence condition. Panel (b) depicts the distribution of excitation energy inferred from  $^{10}\text{Be}$  measured in coincidence with the  $E_\gamma(2^+)$   $\gamma$ -ray transition of  $^{10}\text{Be}$  (black) and with additional coincidence with fission in VAMOS++ (red). The blue and red dashed lines, respectively, indicate the energy  $E_\gamma(2^+)$  and  $B_f + E_\gamma(2^+)$ .

sion events (in coincidence with fission fragments detected in VAMOS++). A threshold for  $\gamma$ -ray emission is evident in the figure, red line, at  $E^* = B_f + E_\gamma(2^+) = 8.94$  MeV. For energy levels below this threshold, when the target-like  $^{10}\text{Be}$  nucleus undergoes excitation, the excitation energy of the complementary  $^{240}\text{Pu}$  system is insufficient to overcome the fission barrier. A similar behavior can be observed from the inclusive transfer distribution, black line, with the threshold at  $E^* = E_\gamma(2^+)$  (shown with blue dashed lines). This measurement of  $\gamma$ -rays in coincidence with  $^{10}\text{Be}$  enables the determination of the probability of exciting target-like nuclei. In this specific case, the probability was measured to be 10 (3) %. This probability can subsequently be accounted for when extracting fission probabilities [4].

## 7. Conclusions and outlook

In the present work, we report on a new detector array, PISTA, designed to characterize fissioning systems populated in multi-nucleon transfer reactions in inverse kinematics. We focus on the measurements providing simultaneously, on an event-by-event basis, the high-resolution excitation energy of the fissioning system and the complete

isotopic identification of the fission fragments. The geometry of the PISTA array enables isotopic identification of the target-like nuclei up to oxygen isotopes and with a mass resolution of 1.1 % (FWHM). An upper limit of  $\sigma_E = 518$  (1) keV, corresponding to  $FWHM_E = 1.217$  (2) MeV, was determined for the excitation energy resolution in the elastic channel when the beam position on the target could not be precisely measured. For events where a fission fragment was detected by the VAMOS++ spectrometer, the target position could be reconstructed. In this case, the corresponding Monte Carlo simulations yielded an excitation energy resolution of  $FWHM_E = 870$  keV. The present results represent a significant improvement compared to previous experimental setups, which will enable, for a wide range of fissioning systems in the actinide region, the extraction of fission probabilities and isotopic fission yields as a function of the excitation energy of the fissioning nucleus, measured with a better precision than with previous setup. In the future, the high spatial segmentation of PISTA, will also enhance the selectivity of event reconstruction of reaction involving multiparticle events like in the reaction channel  $^{12}\text{C}(^{238}\text{U}, ^{242}\text{Pu})^8\text{Be}$ , where the  $^8\text{Be}$  is unbound and decays through the emission of two  $\alpha$  particles. While similar study was already performed with SPIDER in the  $^9\text{Be}(^{238}\text{U}, ^{239}\text{U})^8\text{Be}$  reaction [39], the advantages of PISTA are twofold: (i) the high granularity minimizes the pile-up of the two  $\alpha$  particles in the same strips, and (ii) the improved angular resolution results in an enhanced excitation energy resolution. This will allow the efficient detection of both  $\alpha$  particles and the reconstruction of the excitation energy with unprecedent precision.

## Acknowledgments

We acknowledge the important technical contributions of J. Goupil, L. Menager and A. Giret and the GANIL accelerator staff. L. B.-G. and A.F. acknowledge support from the Région Normandie for the grants supplied under the Réseaux d'Intérêts Normands (RIN) Doctorants 50% and Emergents SAVAV, respectively. This work was partially supported by the Spanish Research State Agency n<sup>o</sup> PID2021-128487NB-I00, by European Union ERDF, by the "María de Maeztu" Units of Excellence program n<sup>o</sup> MDM-2016-0692, by Xunta de Galicia as Centro singular de investigación de Galicia accreditation 2019–2022, and from the "Consolidación e estruturación" n<sup>o</sup> ED431F 2016/002. This work was performed under the auspices of the U.S. Department of Energy by Lawrence Livermore National Laboratory under Contract DE-AC52-07NA27344, and supported in part by the Laboratory Directed Research and Development (LDRD) Program. The views expressed in this article are those of the authors and do not reflect the official policy or position of the U.S. Naval Academy, Department of the Navy, the Department of Defense, or the U.S. Government.

## References

- [1] A. N. Andreyev, K. Nishio, K.-H. Schmidt, [Nuclear fission: a review of experimental advances and phenomenology](#), Reports on Progress in Physics 81 (1) (2017) 016301. [doi:10.1088/1361-6633/aa82eb](https://doi.org/10.1088/1361-6633/aa82eb). URL <https://doi.org/10.1088/1361-6633/aa82eb>
- [2] R. Pérez Sánchez, B. Jurado, V. Méot, O. Roig, M. Dupuis, O. Bouland, D. Denis-Petit, P. Marini, L. Mathieu, I. Tsekhanovich, M. Aïche, L. Audouin, C. Cannes, S. Czajkowski, S. Delpech, A. Görzen, M. Guttormsen, A. Henriques, G. Kessedjian, K. Nishio, D. Ramos, S. Siem, F. Zeiser, [Simultaneous determination of neutron-induced fission and radiative capture cross sections from decay probabilities obtained with a surrogate reaction](#), Phys. Rev. Lett. 125 (2020) 122502. [doi:10.1103/PhysRevLett.125.122502](https://doi.org/10.1103/PhysRevLett.125.122502). URL <https://link.aps.org/doi/10.1103/PhysRevLett.125.122502>
- [3] K. R. Kean, K. Nishio, K. Hirose, M. J. Vermeulen, H. Makii, R. Orlandi, K. Tsukada, A. N. Andreyev, I. Tsekhanovich, S. Chiba, [Validation of the multinucleon transfer method for the determination of the fission barrier height](#), Phys. Rev. C 100 (2019) 014611. [doi:10.1103/PhysRevC.100.014611](https://doi.org/10.1103/PhysRevC.100.014611). URL <https://link.aps.org/doi/10.1103/PhysRevC.100.014611>
- [4] C. Rodríguez-Tajes, F. Farget, X. Derkx, M. Caamaño, O. Delaune, K.-H. Schmidt, E. Clément, A. Dijon, A. Heinz, T. Roger, L. Audouin, J. Benlliure, E. Casarejos, D. Cortina, D. Doré, B. Fernández-Domínguez, B. Jacquot, B. Jurado, A. Navin, C. Paradela, D. Ramos, P. Romain, M. D. Salsac, C. Schmitt, [Transfer reactions in inverse kinematics: An experimental approach for fission investigations](#), Phys. Rev. C 89 (2014) 024614. [doi:10.1103/PhysRevC.89.024614](https://doi.org/10.1103/PhysRevC.89.024614). URL <https://link.aps.org/doi/10.1103/PhysRevC.89.024614>
- [5] K. Hirose, K. Nishio, S. Tanaka, R. Léguillon, H. Makii, I. Nishinaka, R. Orlandi, K. Tsukada, J. Smallcombe, M. J. Vermeulen, S. Chiba, Y. Aritomo, T. Ohtsuki, K. Nakano, S. Araki, Y. Watanabe, R. Tatsuzawa, N. Takaki, N. Tamura, S. Goto, I. Tsekhanovich, A. N. Andreyev, [Role of multichance fission in the description of fission-fragment mass distributions at high energies](#), Phys. Rev. Lett. 119 (2017) 222501. [doi:10.1103/PhysRevLett.119.222501](https://doi.org/10.1103/PhysRevLett.119.222501). URL <https://link.aps.org/doi/10.1103/PhysRevLett.119.222501>

[6] M. J. Vermeulen, K. Nishio, K. Hirose, K. R. Kean, H. Makii, R. Orlandi, K. Tsukada, I. Tsekhanovich, A. N. Andreyev, S. Ishizaki, M. Okubayashi, S. Tanaka, Y. Aritomo, **Measurement of fission-fragment mass distributions in the multinucleon transfer channels of the  $^{18}\text{O} + ^{237}\text{Np}$  reaction**, Phys. Rev. C 102 (2020) 054610. doi:10.1103/PhysRevC.102.054610. URL <https://link.aps.org/doi/10.1103/PhysRevC.102.054610>

[7] D. Ramos, M. Caamaño, F. Farget, C. Rodríguez-Tajes, L. Audouin, J. Benlliure, E. Casarejos, E. Clement, D. Cortina, O. Delaune, X. Derkx, A. Dijon, D. Doré, B. Fernández-Domínguez, G. de France, A. Heinz, B. Jacquot, C. Paradela, M. Rejmund, T. Roger, M.-D. Salsac, C. Schmitt, **Insight into excitation energy and structure effects in fission from isotopic information in fission yields**, Phys. Rev. C 99 (2019) 024615. doi:10.1103/PhysRevC.99.024615. URL <https://link.aps.org/doi/10.1103/PhysRevC.99.024615>

[8] D. Ramos, M. Caamaño, F. Farget, C. Rodríguez-Tajes, A. Lemasson, C. Schmitt, L. Audouin, J. Benlliure, E. Casarejos, E. Clement, D. Cortina, O. Delaune, X. Derkx, A. Dijon, D. Doré, B. Fernández-Domínguez, G. de France, A. Heinz, B. Jacquot, C. Paradela, M. Rejmund, T. Roger, M.-D. Salsac, **Experimental evidence of the effect of nuclear shells on fission dissipation and time**, Phys. Rev. C 107 (2023) L021601. doi:10.1103/PhysRevC.107.L021601. URL <https://link.aps.org/doi/10.1103/PhysRevC.107.L021601>

[9] M. Caamaño, O. Delaune, F. Farget, X. Derkx, K.-H. Schmidt, L. Audouin, C.-O. Bacri, G. Barreau, J. Benlliure, E. Casarejos, A. Chbihi, B. Fernández-Domínguez, L. Gaudefroy, C. Golabek, B. Jurado, A. Lemasson, A. Navin, M. Rejmund, T. Roger, A. Shrivastava, C. Schmitt, **Isotopic yield distributions of transfer- and fusion-induced fission from  $^{238}\text{U} + ^{12}\text{C}$  reactions in inverse kinematics**, Phys. Rev. C 88 (2013) 024605. doi:10.1103/PhysRevC.88.024605. URL <https://link.aps.org/doi/10.1103/PhysRevC.88.024605>

[10] D. Ramos, M. Caamaño, A. Lemasson, M. Rejmund, H. Alvarez-Pol, L. Audouin, J. D. Frankland, B. Fernández-Domínguez, E. Galiana-Baldó, J. Piot, C. Schmitt, D. Ackermann, S. Biswas, E. Clement, D. Durand, F. Farget, M. O. Fregeau, D. Galaviz, A. Heinz, A. Henriques, B. Jacquot, B. Jurado, Y. H. Kim, P. Morfouace, D. Ralet, T. Roger, P. Teubig, I. Tsekhanovich, **Scission configuration of  $^{239}\text{U}$  from yields and kinetic information of fission fragments**, Phys. Rev. C 101 (2020) 034609. doi:10.1103/PhysRevC.101.034609. URL <https://link.aps.org/doi/10.1103/PhysRevC.101.034609>

[11] W. Lang, H.-G. Clerc, H. Wohlfarth, H. Schrader, K.-H. Schmidt, **Nuclear charge and mass yields for  $^{235}\text{U}$ ( $n_{th}$ , f) as a function of the kinetic energy of the fission products**, Nuclear Physics A 345 (1) (1980) 34–71. doi:https://doi.org/10.1016/0375-9474(80)90411-X. URL <https://www.sciencedirect.com/science/article/pii/037594748090411X>

[12] C. Schmitt, A. Guessous, J. Bocquet, H.-G. Clerc, R. Brissot, D. Engelhardt, H. Faust, F. Gönnenwein, M. Mutterer, H. Nifenecker, J. Panicke, C. Ristori, J. Theobald, **Fission yields at different fission-product kinetic energies for thermal-neutron-induced fission of  $^{239}\text{Pu}$** , Nuclear Physics A 430 (1) (1984) 21–60. doi:https://doi.org/10.1016/0375-9474(84)90191-X. URL <https://www.sciencedirect.com/science/article/pii/037594748490191X>

[13] K. Meierbachtol, F. Tovesson, D. Shields, C. Arnold, R. Blakeley, T. Bredeweg, M. Devlin, A. Hecht, L. Heffern, J. Jorgenson, A. Laptev, D. Mader, J. O'Donnell, A. Sierk, M. White, **The spider fission fragment spectrometer for fission product yield measurements**, Nuclear Instruments and Methods in Physics Research Section A: Accelerators, Spectrometers, Detectors and Associated Equipment 788 (2015) 59–66. doi:https://doi.org/10.1016/j.nima.2015.02.032. URL <https://www.sciencedirect.com/science/article/pii/S0168900215002314>

[14] Deshayes, Quentin, Berthoumieux, Eric, Doré, Diane, Thulliez, Loic, Combet, Michel, Kebbiri, Mariam, Legou, Philippe, Marcel, Alain, Mols, Jean-Philippe, Frégeau, Marc-Olivier, Herlant, Sébastien, Ledoux, Xavier, Pancin, Julien, Falstaff, an apparatus to study fission fragment properties first arm results, EPJ Web Conf. 239 (2020) 05012. doi:10.1051/epjconf/202023905012. URL <https://doi.org/10.1051/epjconf/202023905012>

[15] M. Gooden, C. Arnold, J. Becker, C. Bhatia, M. Bhike, E. Bond, T. Bredeweg, B. Fallin, M. Fowler, C. Howell, J. Kelley, Krishchayan, R. Macri, G. Russel, C. Ryan, S. Sheets, M. Stoyer, A. Tonchev, W. Tornow, D. Vieira, J. Wilhelmy, **Energy dependence of fission product yields from  $^{235}\text{U}$ ,  $^{238}\text{U}$  and  $^{239}\text{Pu}$  for incident neutron energies between 0.5 and 14.8 mev**, Nuclear Data Sheets 131 (2016) 319–356, special Issue on Nuclear Reaction Data. doi:https://doi.org/10.1016/j.nds.2015.12.006.

URL <https://www.sciencedirect.com/science/article/pii/S009037521500071X>

[16] M. E. Gooden, R. C. Malone, T. A. Bredeweg, E. M. Bond, S. W. Finch, C. R. Howell, Krishichayan, A. P. D. Ramirez, J. A. Silano, M. A. Stoyer, A. P. Tonchev, W. Tornow, D. Vieira, J. B. Wilhelmy, **Energy dependence of fission product yields in the second-chance fission region**, Phys. Rev. C 109 (2024) 044604. doi:[10.1103/PhysRevC.109.044604](https://doi.org/10.1103/PhysRevC.109.044604). URL <https://link.aps.org/doi/10.1103/PhysRevC.109.044604>

[17] A. Tonchev, J. Silano, A. Ramirez, R. Malone, M. Stoyer, M. Gooden, T. Bredeweg, D. Vieira, J. Wilhelmy, S. Finch, C. Howell, W. Tornow, **Energy dependence of chain fission product yields from neutron-induced fission of  $^{235}\text{U}$ ,  $^{238}\text{U}$ , and  $^{239}\text{Pu}$** , Nuclear Data Sheets 202 (2025) 12–29. doi:<https://doi.org/10.1016/j.nds.2025.04.002>. URL <https://www.sciencedirect.com/science/article/pii/S0090375225000353>

[18] K.-H. Schmidt, S. Steinhäuser, C. Böckstiegel, A. Grewe, A. Heinz, A. Junghans, J. Benlliure, H.-G. Clerc, M. de Jong, J. Müller, M. Pfützner, B. Voss, **Relativistic radioactive beams: A new access to nuclear-fission studies**, Nuclear Physics A 665 (3) (2000) 221–267. doi:[https://doi.org/10.1016/S0375-9474\(99\)00384-X](https://doi.org/10.1016/S0375-9474(99)00384-X). URL <https://www.sciencedirect.com/science/article/pii/S037594749900384X>

[19] A. Chatillon, J. Taïeb, H. Alvarez-Pol, L. Audouin, Y. Ayyad, G. Bélier, J. Benlliure, G. Boutoux, M. Caamaño, E. Casarejos, D. Cortina-Gil, A. Ebran, F. Farget, B. Fernández-Domínguez, T. Gorbinet, L. Grente, A. Heinz, H. T. Johansson, B. Jurado, A. Kelić Heil, N. Kurz, B. Laurent, J.-F. Martin, C. Nociforo, C. Paradela, E. Pellereau, S. Pietri, A. Prochazka, J. L. Rodríguez-Sánchez, D. Rossi, H. Simon, L. Tassan-Got, J. Vargas, B. Voss, H. Weick, **Evidence for a new compact symmetric fission mode in light thorium isotopes**, Phys. Rev. Lett. 124 (2020) 202502. doi:[10.1103/PhysRevLett.124.202502](https://doi.org/10.1103/PhysRevLett.124.202502). URL <https://link.aps.org/doi/10.1103/PhysRevLett.124.202502>

[20] E. Pellereau, J. Taïeb, A. Chatillon, H. Alvarez-Pol, L. Audouin, Y. Ayyad, G. Bélier, J. Benlliure, G. Boutoux, M. Caamaño, et al., Accurate isotopic fission yields of electromagnetically induced fission of  $^{238}\text{U}$  measured in inverse kinematics at relativistic energies, Physical Review C 95 (5) (2017) 054603.

[21] R. Léguillon, K. Nishio, K. Hirose, H. Makii, I. Nishinaka, R. Orlandi, K. Tsukada, J. Smallcombe, S. Chiba, Y. Aritomo, T. Ohtsuki, R. Tatsuzawa, N. Takaki, N. Tamura, S. Goto, I. Tsekhanovich, C. Petrache, A. Andreyev, **Fission fragments mass distributions of nuclei populated by the multinucleon transfer channels of the  $^{180}\text{O}+^{232}\text{Th}$  reaction**, Physics Letters B 761 (2016) 125–130. doi:<https://doi.org/10.1016/j.physletb.2016.08.010>. URL <https://www.sciencedirect.com/science/article/pii/S0370269316304300>

[22] M. Rejmund, B. Lecornu, A. Navin, C. Schmitt, S. Damoy, O. Delaune, J. Enguerrand, G. Fremont, P. Gangnant, L. Gaudefroy, B. Jacquot, J. Pancin, S. Pullanhiotan, C. Spitaels, **Performance of the improved larger acceptance spectrometer: Vamos++**, Nuclear Instruments and Methods in Physics Research Section A: Accelerators, Spectrometers, Detectors and Associated Equipment 646 (1) (2011) 184–191. doi:<https://doi.org/10.1016/j.nima.2011.05.007>. URL <https://www.sciencedirect.com/science/article/pii/S0168900211008515>

[23] D. Suzuki, **Missing mass spectroscopy on oxygen isotopes beyond the proton-drip line: mirror symmetry of nuclear shell evolution**, Eur. Phys. J. A 48 (9) (2012) 130. URL <https://doi.org/10.1140/epja/i2012-12130-6>

[24] M. Vandebruck, A. Lemasson, M. Rejmund, G. Fremont, J. Pancin, A. Navin, C. Michelagnoli, J. Goupil, C. Spitaels, B. Jacquot, **Dual position sensitive mwpc for tracking reaction products at vamos++**, Nuclear Instruments and Methods in Physics Research Section A: Accelerators, Spectrometers, Detectors and Associated Equipment 812 (2016) 112–117. doi:<https://doi.org/10.1016/j.nima.2015.12.040>. URL <https://www.sciencedirect.com/science/article/pii/S0168900215016113>

[25] J. Simpson, F. Azaiez, G. de France, G. Fouan, J. Gerl, et al., **The EXOGAM array: A radioactive beam gamma-ray spectrometer**, Acta Physica Hungarica New Series-Heavy ion 11 (2000) 159–188.

[26] J. Frankland, N. Le Neindre, M. Henri, C. Gouyet, R. Revenko, Q. Fable, D. Gruyer, R. Bourgault, A. Chbihi, T. Genard, J. Lemarié, O. Lopez, Q. Beaudouin, B. Borderie, P. Bourgault, C. Ciampi, I. Dekhissi, V. Godefroid, M. La Commara, L. Leterrier, E. Loubeau, F. Marie-Sailenfest, C. Nicolle, F. Noury, M. Parlog, J. Perronnel, M. Prieur, A. Rebillard-Soulié, L. Rousseau, A. Valente, G. Verde, **Digital electronics upgrade of the in-dra charged particle detection array and resulting performance improvements**, Nuclear Instruments and Methods in Physics Research Section A: Accelerators, Spectrometers, Detectors and Associated Equipment (2025) 170908 doi:<https://doi.org/10.1016/j.nima.2025.170908>

//doi.org/10.1016/j.nima.2025.170908.  
 URL <https://www.sciencedirect.com/science/article/pii/S0168900225007107>

[27] mesytec, mesytec mdpp-16 module, <https://www.mesytec.com/products/nuclear-physics/MDPP-16.html>.

[28] mesytec, mesytec mmr system, <https://www.mesytec.com/products/nuclear-physics/MMR.html>.

[29] mesytec, mesytec mvlc module, <https://www.mesytec.com/products/nuclear-physics/MVLC.html>.

[30] X. Grave, R. Canedo, J.-F. Clavelin, S. Du, E. Legay, Narval a modular distributed data acquisition system with ada 95 and rtai, in: 14th IEEE-NPSS Real Time Conference, 2005., 2005, pp. 5 pp.–. doi:10.1109/RTC.2005.1547454.

[31] M. Bellato, D. Bortolato, J. Chavas, R. Isocrate, G. Rampazzo, A. Triossi, D. Bazzacco, D. Mengoni, F. Recchia, Sub-nanosecond clock synchronization and trigger management in the nuclear physics experiment agata, Journal of Instrumentation 8 (07) (2013) P07003. doi:10.1088/1748-0221/8/07/P07003.  
 URL <https://dx.doi.org/10.1088/1748-0221/8/07/P07003>

[32] C. Houarner, A. Boujrad, M. Tripone, M. Bezard, M. Blaizot, P. Bourgault, S. Coudert, B. Duclos, F. Egea, G. de France, A. Gadea, A. Lemasson, L. Martina, C. Maugeais, J. Pancin, B. Raine, F. Saillant, A. Triossi, G. Wittwer, Numexo2: a versatile digitizer for nuclear physics, Journal of Instrumentation 20 (05) (2025) T05004. doi:10.1088/1748-0221/20/05/T05004.  
 URL <https://dx.doi.org/10.1088/1748-0221/20/05/T05004>

[33] Mesytec VME data acquisition software, <https://www.mesytec.com/downloads/mvme.html>.

[34] J. Frankland, A. Lemasson, Mfmerger (2024). doi:10.5281/zenodo.13374037.  
 URL <https://doi.org/10.5281/zenodo.13374037>

[35] E850 Collaboration, E850 GANIL dataset (2024). doi:10.26143/ganil-2023-e850\_21.

[36] M. Rejmund, A. Lemasson, Analysis of atomic charge state and atomic number for vamos++ magnetic spectrometer using deep neural networks and fractionally labelled events, Journal of Instrumentation 20 (08) (2025) P08022. doi:10.1088/1748-0221/20/08/P08022.  
 URL <https://doi.org/10.1088/1748-0221/20/08/P08022>

[37] F. Hubert, R. Bimbot, H. Gauvin, Range and stopping-power tables for 2.5–500 mev/nucleon heavy ions in solids, Atomic Data and Nuclear Data Tables 46 (1) (1990) 1–213. doi:[https://doi.org/10.1016/0092-640X\(90\)90001-Z](https://doi.org/10.1016/0092-640X(90)90001-Z).  
 URL <https://www.sciencedirect.com/science/article/pii/0092640X9090001Z>

[38] S. Bjørnholm, J. E. Lynn, The double-humped fission barrier, Rev. Mod. Phys. 52 (1980) 725–931. doi:10.1103/RevModPhys.52.725.  
 URL <https://link.aps.org/doi/10.1103/RevModPhys.52.725>

[39] D. Ramos, M. Caamaño, A. Lemasson, M. Rejmund, L. Audouin, H. Álvarez-Pol, J. D. Frankland, B. Fernández-Domínguez, E. Galiana-Baldó, J. Piot, D. Ackermann, S. Biswas, E. Clement, D. Durand, F. Farget, M. O. Fregeau, D. Galaviz, A. Heinz, A. I. Henriques, B. Jacquot, B. Jurado, Y. H. Kim, P. Morfouace, D. Ralet, T. Roger, C. Schmitt, P. Teubig, I. Tsekhanovich, First direct measurement of isotopic fission-fragment yields of  $^{239}\text{U}$ , Phys. Rev. Lett. 123 (2019) 092503. doi:10.1103/PhysRevLett.123.092503.  
 URL <https://link.aps.org/doi/10.1103/PhysRevLett.123.092503>